ACS Energy LETTERS

http://pubs.acs.org/journal/aelccp

# Cesium Manganese Bromide Nanocrystal Sensitizers for Broadband Vis-to-NIR Downshifting

Houman Bahmani Jalali, Andrea Pianetti, Juliette Zito, Muhammad Imran, Marta Campolucci, Yurii P. Ivanov, Federico Locardi, Ivan Infante, Giorgio Divitini, Sergio Brovelli, Liberato Manna,* and Francesco Di Stasio*

Cite This: *ACS Energy Lett.* 2022, 7, 1850−1858

Read Online

ACCESS | Metrics & More | Article Recommendations | Supporting Information

**ABSTRACT:** Simultaneously achieving both broad absorption and sharp emission in the near-infrared (NIR) is challenging. Coupling of an efficient absorber such as lead halide perovskites to lanthanide emissive species is a promising way to meet the demands for visible-to-NIR spectral conversion. However, lead-based perovskite sensitizers suffer from relatively narrow absorption in the visible range, poor stability, and toxicity. Herein, we introduce a downshifting configuration based on lead-free cesium manganese bromide nanocrystals acting as broad visible absorbers coupled to sharp emission in the NIR-I and NIR-II spectral regions. To achieve this, we synthesized $CsMnBr_3$ and $Cs_3MnBr_5$ nanocrystals and attempted to dope them with a series of lanthanides, achieving success only with $CsMnBr_3$. The correlation of the lanthanide emission to the $CsMnBr_3$ visible absorption was confirmed with steady-state excitation spectra and time-resolved photoluminescence measurements, whereas the mechanism of downconversion from the $CsMnBr_3$ matrix to the lanthanides was understood by density functional theory calculations. This study shows that lead-free metal halides with an appropriate phase are effective sensitizers for lanthanides and offer a route to efficient downshifting applications.

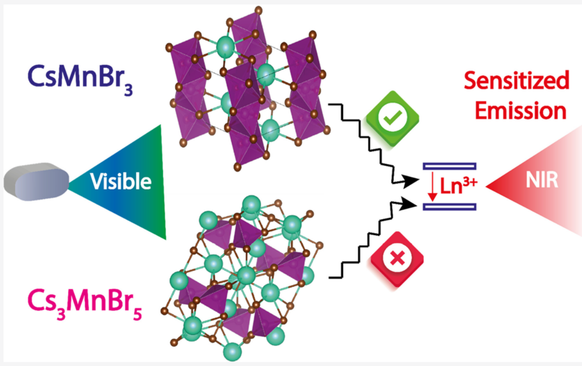


Downshifting luminescence is a single-photon process that converts absorbed high-energy photons to low-energy ones,[1] and it is employed in a broad range of applications including solar cells,[1−3] luminescent solar concentrators,[4] near-infrared light emitting diodes (NIR LEDs),[5] bioimaging,[6−8] and biosensors.[9,10] A common strategy for downshifting luminescence is based on a trivalent lanthanide ($Ln^{3+}$) ion as the emission center and a sensitizer as the light absorption center. Lanthanide ions have several interesting properties as potential sensitizers, such as ladder-like electronic states and long radiative lifetimes (10 μs−10 ms),[11−14] which can promote luminescence conversion. However, their progress as downshifters is limited since $Ln^{3+}$ ions (e.g., $Yb^{3+}$, $Er^{3+}$, $Tm^{3+}$, $Nd^{3+}$ and $Ho^{3+}$) have narrow absorption widths as well as very small absorption cross sections due to their electric-dipole-forbidden 4f→4f transitions.[15,16] Although traditional semiconductor nanocrystals (NCs) such as CdSe,[17,18] InP,[19−22] and $Ag_2Se$[23] have a high absorption cross section and can be used as host materials, their covalently bonded rigid lattices complicate the doping process with lanthanide ions.[11,24] Instead, halide perovskites are ideal for substitutional doping due to the softness and strong ionicity of their lattice, and additionally they offer very high absorption cross sections.[2,5,25−29] Various reports have shown that in lead halide perovskites a downshifted luminescence in the visible and infrared spectral range can be achieved through doping with divalent cations (for instance, $Cd^{2+}$, $Mn^{2+}$),[30,31] trivalent cations ($Ln^{3+}$),[27,32,33] or a combination thereof.[28] Yet, the toxicity and stability issues of lead-based perovskites are a strong drive toward alternative metal halides,[34−37] and several Pb-free double perovskites (e.g., $Cs_2AgInCl_6$,[38−40] $Cs_2AgBiX_6$ (X = Cl, Br),[39,41] and $Cs_3Bi_2Br_9$[39]) have been synthesized and tested as hosts. Furthermore, most of these materials absorb only in the blue-

**Received:** February 9, 2022
**Accepted:** April 19, 2022

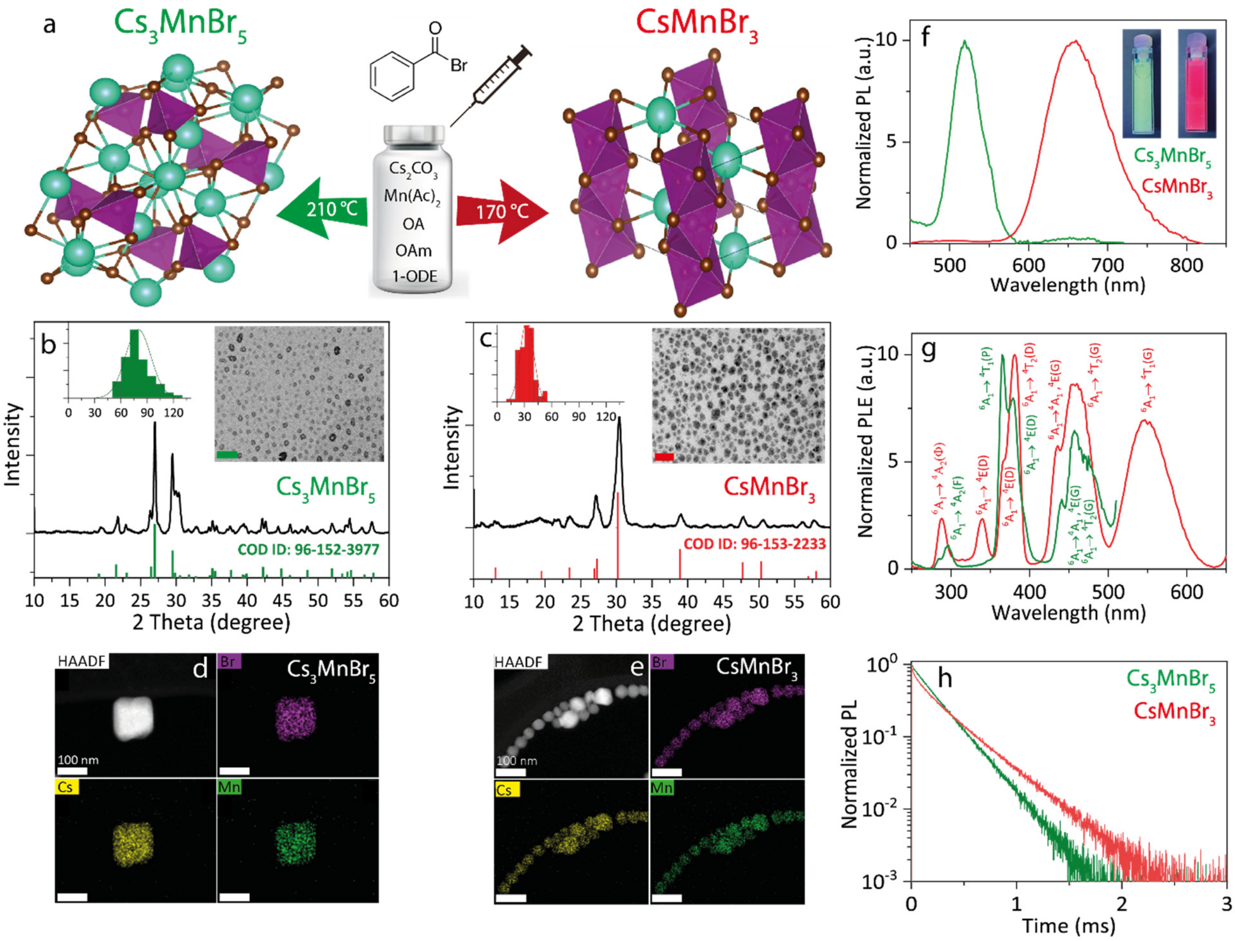


**Figure 1. Structural and optical analyses of $CsMnBr_3$ and $Cs_3MnBr_5$ NCs. (a) Schematic representation of the synthesis procedure and standard depiction (Cs = green, Mn = violet, and Br = brown) of the $Cs_3MnBr_5$ and $CsMnBr_3$ structures. (b) XRD pattern and reference pattern COD ID: 96-152-3977 of the $Cs_3MnBr_5$ NCs (right inset: TEM image, scale bar = 400 nm; left inset: particle size distribution). (c) XRD pattern and reference pattern COD ID: 96-153-2233 of the $CsMnBr_3$ NCs (right inset: TEM image, scale bar = 100 nm; left inset: particle size distribution). HAADF STEM image and EDS maps of (d) $Cs_3MnBr_5$ and (e) $CsMnBr_3$ NCs. (f) Photoluminescence (PL) spectra of the $Cs_3MnBr_5$ (green, $\lambda_{exc}$ = 380 nm) and $CsMnBr_3$ (red, $\lambda_{exc}$ = 380 nm) NCs dispersed in toluene. Inset: Photographs of the $Cs_3MnBr_5$ and $CsMnBr_3$ NC solutions under UV light. (g) Photoluminescence excitation (PLE) spectra of the $Cs_3MnBr_5$ (green, $\lambda_{em}$ = 522 nm) and $CsMnBr_3$ (red, $\lambda_{em}$ = 661 nm) NCs dispersed in tolouene. (h) PL time decay of $Cs_3MnBr_5$ (green, $\lambda_{em}$ = 522 nm) and $CsMnBr_3$ (red, $\lambda_{em}$ = 661 nm) NCs dispersed in toluene.**

visible range (<500 nm).[38−41] Therefore, it is highly desirable to increase absorptivity and overall broadening of the absorption spectrum of the downshifter to the visible spectral range.

The recently reported cesium manganese bromide NCs offer several appealing properties and hold great potential as sensitizers.[42−44] The advantages of cesium manganese bromide NCs include (i) a broad absorption spectrum covering the visible spectral range,[42,44] (ii) high absorption coefficients ($\varepsilon_{544\ nm}$ = 83.6 $M^{-1}\cdot cm^{-1}$ for $CsMnBr_3$[42]), and (iii) significantly reduced toxicity compared to Pb-based compounds. Also, recent works have shown that the luminescence of these materials can be tuned by changing the coordination geometry of the $Mn^{2+}$ ions since, depending on whether such coordination is tetrahedral or octahedral, the emission is either in the green or in the red spectral range, respectively.[44] Nonetheless, it is significantly challenging to control and engineer the colloidal synthesis of cesium manganese bromide NCs due to the presence of energetically similar competing phases.[42]

Herein, we report phase-selective syntheses of colloidal $Cs_3MnBr_5$ NCs and $CsMnBr_3$ NCs exhibiting green and red luminescence, respectively. We then attempt to dope both phases with various NIR-emitting lanthanide ions. Interestingly, our results show that $CsMnBr_3$ can be doped successfully with $Nd^{3+}$, $Er^{3+}$, $Tm^{3+}$, and $Yb^{3+}$, while $Cs_3MnBr_5$ is inert toward all dopants due to the difficulty of lanthanides incorporation in tetrahedrally coordinated environments. Lanthanide-doped $CsMnBr_3$ NCs demonstrate emission in the NIR-I (∼800−900 nm)[45] and NIR-II (1000−1700 nm)[45] spectral regions. These findings agree with our computational analysis on both cesium manganese bromide systems. Our study demonstrates a versatile sensitizer for downshifting luminescence of lanthanides, and it provides new opportunities for applications of lanthanide-doped nanosystems.

**Synthesis of $Cs_3MnBr_5$ and $CsMnBr_3$ NCs.** As mentioned earlier, the synthesis of phase-pure cesium manganese bromide-based NCs is more challenging than that of classical lead halide perovskite NCs due to the presence of different competing phases that can be easily formed in the $CsBr-MnBr_2$ phase diagram, such as $CsMnBr_3$, $Cs_3MnBr_5$,


https://doi.org/10.1021/acsenergylett.2c00311
ACS Energy Lett. 2022, 7, 1850−1858

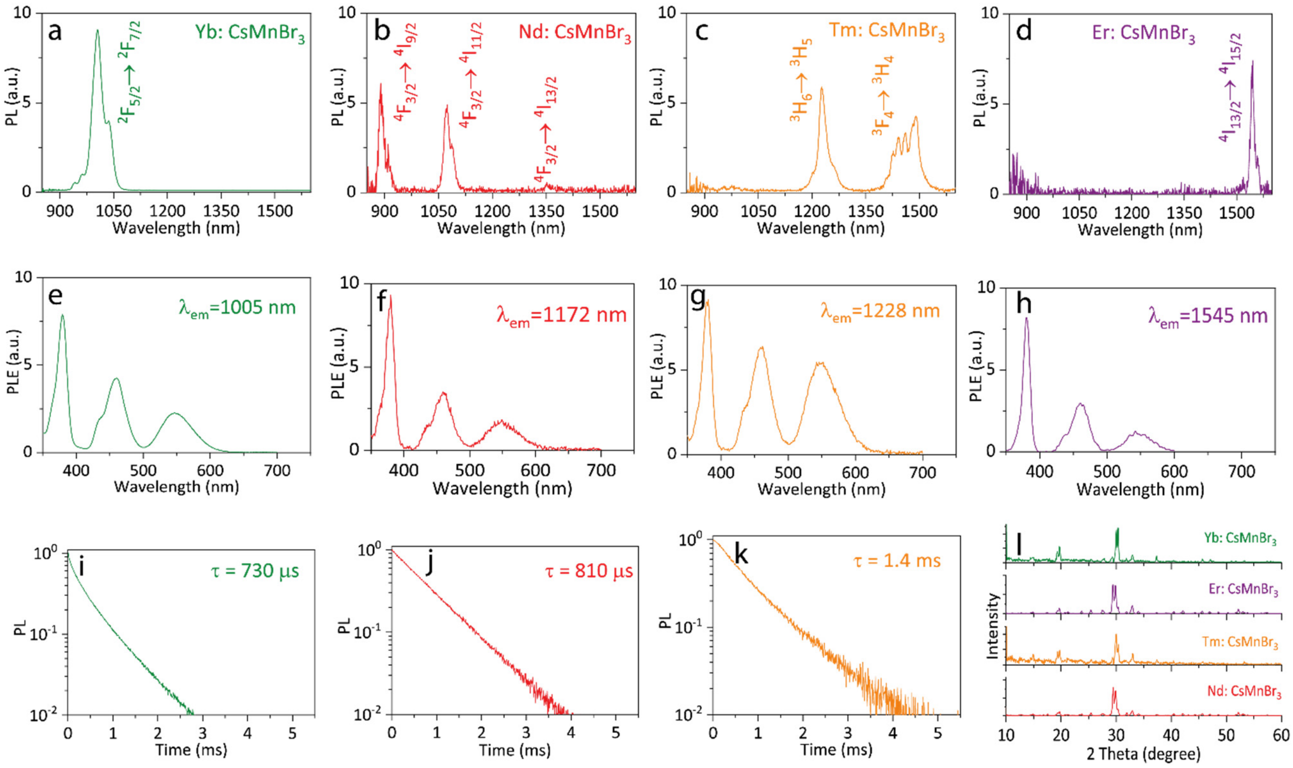


**Figure 2. Vis-to-NIR downshifting using $Ln^{3+}$-doped $CsMnBr_3$ NCs. (a) Yb-doped, (b) Nd-doped, (c) Tm-doped, and (d) Er-doped $CsMnBr_3$ NCs ($\lambda_{exc}$ = 550 nm). PLE spectra of (e) Yb-doped ($\lambda_{em}$ = 1005 nm), (f) Nd-doped ($\lambda_{em}$ = 1172 nm), (g) Tm-doped ($\lambda_{em}$ = 1228 nm), and (h) Er-doped ($\lambda_{em}$ = 1545 nm) $CsMnBr_3$ NCs. PL decay curves of (i) Yb-doped ($\lambda_{det}$ = 990 nm), (j) Nd-doped ($\lambda_{det}$ = 895 nm), and (k) Tm-doped ($\lambda_{det}$ = 1485 nm) $CsMnBr_3$ NCs ($\lambda_{exc}$= 355 nm). (l) XRD patterns of the $CsMnBr_3$ NCs doped with Yb, Er, Tm, and Nd ions.**

and $Cs_2MnBr_4$.[46] In a recent study, $CsMnBr_3$ and $Cs_3MnBr_5$ NCs were synthesized in a Schlenk line system using the highly reactive trimethylbromosilane as the bromide source.[44] As a safer synthesis route, we prepared here $Cs_3MnBr_5$ and $CsMnBr_3$ NCs using a modified version of our previously developed benzoyl halide-based synthesis approach, which enables independent tunability of the concentration of metal cations, halide ions, and surfactants.[47−49] Briefly, NCs were synthesized by injecting benzoyl bromide into a solution of cesium and manganese oleates in the presence of oleylamine (see scheme in Figure 1a). We found that $CsMnBr_3$ and $Cs_3MnBr_5$ NCs can be separately prepared, each with high phase purity, under optimized sets of reaction conditions (precursors with tailored ratios, reaction temperature, and time; see the details in the Experimental Methods). X-ray diffraction (XRD) analysis indicates that $CsMnBr_3$ NCs have a hexagonal crystal structure ($P6_3/mmc$ space group) formed by chains of face-sharing $[MnBr_6]$ octahedra that are charge-balanced by cesium ions along the *c*-axis (Figure 1a). The $Cs_3MnBr_5$ NCs has instead a tetragonal crystal structure formed by isolated $[MnBr_4]$ tetrahedra (each $Mn^{2+}$ ion is bound in a tetrahedral configuration to four $Br^-$ ions) and stabilized by cesium ions ($I4/mcm$ space group, Figure 1a). These results are consistent with existing literature on bulk $CsMnBr_3$[50,51] and $Cs_3MnBr_5$[52] crystals. According to transmission electron microscopy (TEM) analysis, the NCs has a mean size of 78 ± 14 nm (Figure 1b, inset) and 33 ± 7 nm (Figure 1c, inset) for $Cs_3MnBr_5$ and $CsMnBr_3$ NCs, respectively. The much larger size of the $Cs_3MnBr_5$ NCs can be attributed to the higher injection temperature (210 °C) required in their synthesis compared to the $CsMnBr_3$ NCs case (170 °C). HAADF STEM images in combination with EDS mapping confirm compatible compositions for $Cs_3MnBr_5$ (Figure 1d) and $CsMnBr_3$ NCs (Figure 1e and Table S1).

The optical properties and electronic structure of manganese halides are due to electronic transitions localized in the $[MnBr_x]$ ($x$ = 4, 6) polyhedra that are dominated by d-d transitions within the Mn cations mixed with some orbital contribution from the nearby 4p of the Br ions. These excitations are typically spin and parity forbidden;[53−56] nevertheless, exchange coupling as well as spin−orbit coupling are responsible for the relaxation of spin selection rules in antiferromagnetic manganese halides.[56] These optical properties can be tuned by changing the coordination geometry around the $Mn^{2+}$ ions and the Mn−Mn distance.[57,58] In particular, tetrahedrally coordinated $Mn^{2+}$ exhibits green emission,[55] while octahedrally coordinated $Mn^{2+}$ exhibits red emission.[59,60] We studied the steady-state optical properties in colloidal dispersions to reconfirm the presence of $Cs_3MnBr_5$ and $CsMnBr_3$ NCs. $Cs_3MnBr_5$ NCs features green emission centered at 522 nm, while the $CsMnBr_3$ NCs shows red emission centered at 661 nm (Figure 1f), and both phases show photoluminescence quantum yields (PLQYs) in the range of 33 ± 4%, which decreases to 8 ± 2% after storage in the ambient air for 10 days (relative humidity ∼40%). Importantly, the $Cs_3MnBr_5$ NC solution shows only negligible emission in the red spectral region compared to the literature. In fact, the only reported $Cs_3MnBr_5$ NCs' photoluminescence to date had two intense emissions around 520 and 660 nm,[44] indicating the actual presence of both $Cs_3MnBr_5$ and CsMnBr phases in that sample. The optical absorption spectra for the $Cs_3MnBr_5$ and $CsMnBr_3$ NCs prepared by us are reported in


https://doi.org/10.1021/acsenergylett.2c00311
ACS Energy Lett. 2022, 7, 1850−1858

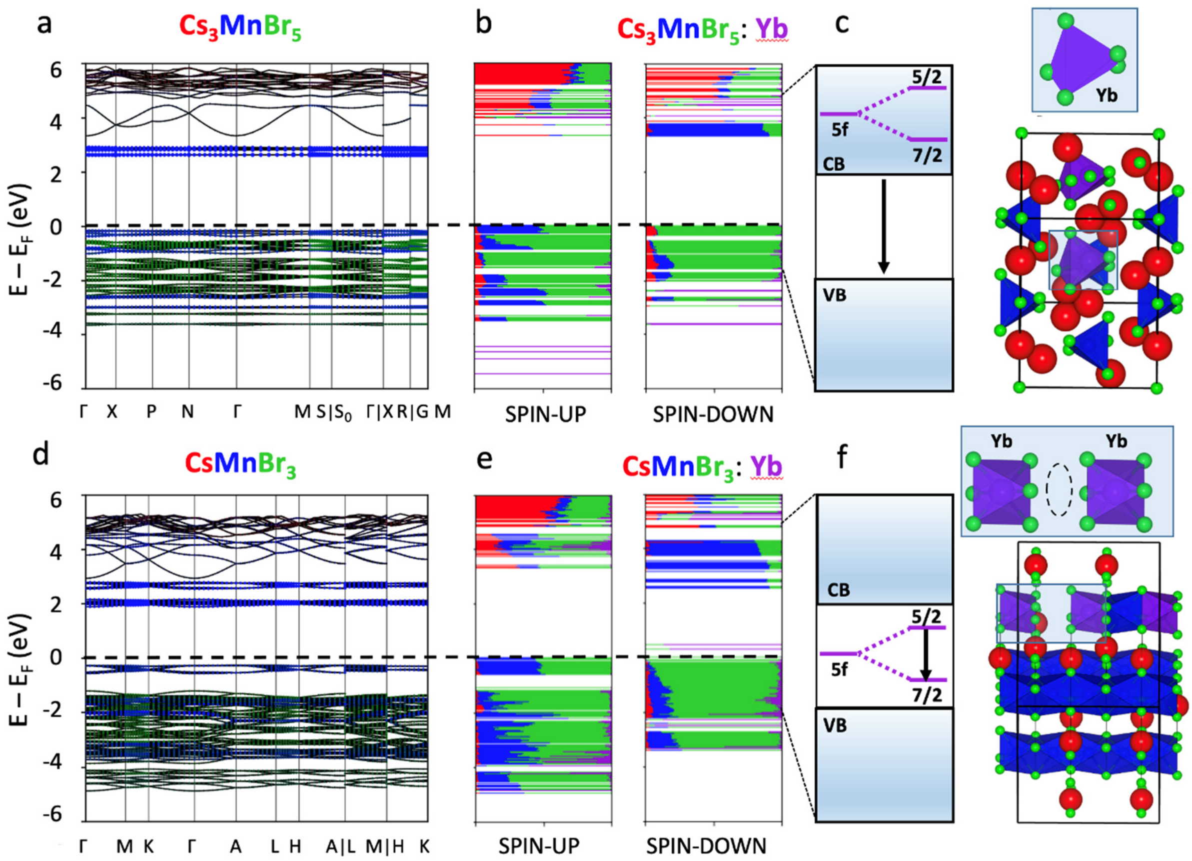


**Figure 3. Density functional theory analyses of undoped and doped $Cs_3MnBr_5$ and $CsMnBr_3$ systems. (a) Element projected band structure of the relaxed $Cs_3MnBr_5$ unit cell calculated at the DFT/PBE level of theory. (b) Electronic structure of the Yb-doped $Cs_3MnBr_5$ 2×2×2 supercell (shown on the right) computed at the Γ point at the DFT/PBE level of theory. Each orbital is represented in real space and decomposed according to each atom type. (c) Scheme of the expected position for Yb $5f_{5/2}$ and $5f_{7/2}$ orbitals upon spin−orbit mixing. (d), (e), and (f) are the same as (a), (b), and (c), respectively, but for the $CsMnBr_3$ system.**

Figure S1, while Figure 1g displays the photoluminescence excitation (PLE) spectra, in which the d-d transition of the $Mn^{2+}$ ion in $d^5$ configuration and different excitation states funnel the excitation to the same transition ($^6A_1 \rightarrow ^4T_1(G)$) for both tetrahedral $Cs_3MnBr_5$[55] and octahedral $CsMnBr_3$[59,60] NCs (Figure 1g). The PL time decays of $CsMnBr_3$ and $Cs_3MnBr_5$ NC solutions reveal a single exponential kinetics at room temperature. The $Cs_3MnBr_5$ NCs, emitting at 522 nm, decay faster ($\tau$ = 170 $\mu$s) than the $CsMnBr_3$ NCs ($\tau$ = 235 $\mu$s), the latter emitting at 661 nm, which is in agreement with the literature (Figure 1h, Table S2).[44] Interestingly, no excitation-dependent PL decay lifetime has been observed for $CsMnBr_3$ and $Cs_3MnBr_5$ NCs (excitation at 532 nm vs 355 nm).

**Vis-to-NIR Downshifting Using $Ln^{3+}$-Doped $CsMnBr_3$ NCs.** Sensitizers hosting different types of lanthanides and efficiently absorbing in the visible spectral range are highly desirable for downshifting applications.[19,61] This motivated us to investigate the performance of both $CsMnBr_3$ and $Cs_3MnBr_5$ NCs as sensitizers. For that, we attempted doping with different lanthanide dopants, including $Yb^{3+}$, $Nd^{3+}$, $Tm^{3+}$, and $Er^{3+}$, via a facile synthesis route (see Experimental Methods), on both NC systems. Energy-dispersive X-ray spectroscopy (EDS) revealed unsuccessful doping of the $Cs_3MnBr_5$ NCs (Figure S2). The apparently ineffective doping of $Cs_3MnBr_5$ NCs with lanthanides might stem from the difficulty to incorporate lanthanides (preferring CN ≥ 6[62−64]) in a tetrahedrally coordinated environment or by the lack of a favorable energy alignment between the dopant and the Mn matrix (*vide infra*).[11] On the other hand, $CsMnBr_3$ NCs were successfully doped by $Yb^{3+}$, $Nd^{3+}$, $Tm^{3+}$, and $Er^{3+}$ (Figures S3−S6). However, for the case of $CsMnBr_3$, two $Ln^{3+}$ ions can, in principle, substitute three $Mn^{2+}$ ions, generating a cation vacancy ($V_{Mn}$),[65] as was reported for $CsMnCl_3$[66,67] and $CsPbX_3$.[2,3,26,68−72] The higher content of Nd (1.22 at.%) compared to Yb (1.19 at.%), Er (1.02 at.%), and Tm (0.89 at.%) that we could introduce in the NCs can be explained by the lower ionic radius mismatch between $Mn^{2+}$ (97 ppm[73]) and $Nd^{3+}$ (98.3 ppm[74]) compared to $Er^{3+}$ (89 ppm[74]), $Tm^{3+}$ (87 ppm[75]), and $Yb^{3+}$ (86 ppm[76]). In addition, XRD patterns of lanthanide-doped $CsMnBr_3$ NCs indicate no extra diffraction peaks nor any notable shift compared to undoped $CsMnBr_3$ NCs (Figure 2l) due to the low amount of lanthanides (<1.5 at.%) that could be introduced in the lattice, as reported for Er-doped[27] and Yb-doped[26] $CsPbCl_3$ NCs.

We observed NIR emission features via excitation in the visible spectral range (550 nm) for $CsMnBr_3$ NCs doped with $Yb^{3+}$, $Nd^{3+}$, $Tm^{3+}$, and $Er^{3+}$ (Figure 2a−d) having NIR PLQYs in the range of 0.24−1.1% (see Table S4). Furthermore, the lanthanide-doped $CsMnBr_3$ NCs have the same PLE profile as the undoped $CsMnBr_3$ NCs toward all types of dopants (Figure 2e−h). This suggests that lanthanide NIR emission is triggered by excitation of the host $CsMnBr_3$ NCs. This phenomenon is in agreement with the efficient energy transfer from $Mn^{2+}$ commonly observed in lanthanide-doped bulk


https://doi.org/10.1021/acsenergylett.2c00311
ACS Energy Lett. 2022, 7, 1850−1858

$CsMnBr_3$,[56,77,78] $CsMnCl_3$,[56,79] and $CsMnI_3$.[56,77] In our case, since the NCs are small and the doping level is relatively higher (around 1 part per 80, 84, 100, and 112 for Nd,- Yb-, Er-, and Tm-doped $CsMnBr_3$, respectively) than the one reported for doped $CsMnBr_3$ (1 part per 1000 for Nd:$CsMnBr_3$[80] and 1 part per 500 for Er:$CsMnBr_3$[77]), energy transfer does not require migration of excitation among all Mn sites. For this reason, the introduction of lanthanides quenches completely the emission from the Mn-centered d-d transition of $CsMnBr_3$ at 661 nm. The near-infrared PL time decays show a single-exponential decay with a lifetime of 810, 730, and 1400 $\mu$s for Nd:$CsMnBr_3$, Yb:$CsMnBr_3$, and Tm:$CsMnBr_3$, respectively (Figure 2i–k, Table S3), which also shows that there is no interdoping effect.

**Computational Analysis of $Ln^{3+}$-Doped $CsMnBr_3$ and $Cs_3MnBr_5$ NCs.** To disentangle the mechanism of emission of lanthanide-doped $CsMnBr_3$ and $Cs_3MnBr_5$ NCs, we carried out DFT calculations. First, the band structures of both undoped $CsMnBr_3$ and $Cs_3MnBr_5$ systems were computed at the DFT/PBE level (Figure 3a,d). In these band structures, the flat conduction and valence band edges are dominated by localized Mn half-filled d orbitals, which confirms that the emission arises from the d-d transition of $Mn^{2+}$ ion in $d^5$ configuration (see Figure 1d,e). Our calculations also indicate that both systems slightly favor an antiferromagnetic behavior (see the "Density Functional Theory calculations" paragraph in the Experimental Methods). For the doped systems, we decided to analyze the Yb doping since Yb presents only one unpaired electron that gives origin to one emission line ($^2F_{5/2} \rightarrow {}^2F_{7/2}$) upon spin–orbit mixing and greatly facilitates the interpretation of the results. To improve the convergence of our DFT calculations, we considered spin-free calculations, i.e., no spin–orbit coupling: we doubled the size of the unit cell to perform the computation only in the Γ point and assumed a purely ferromagnetic behavior, with all unpaired electrons in Mn and Yb occupying the spin-up orbitals. We consider this latter approximation as valid due to the very small energetic difference from the purely antiferromagnetic systems. We do, however, warn the reader that based on the above approximations and considering that DFT has limitations in describing f-orbitals with high precision, we aim to acquire only a purely qualitative description of the doped systems.

Starting with the density of states of the $Cs_3MnBr_5$:Yb system (Figure 3b), composed of disconnected tetrahedra, we can notice that even in the case when Yb is incorporated in $Cs_3MnBr_5$, the occupied f-orbitals of Yb lie very deep in the valence band, whereas the only unoccupied f orbital (spin-down) is found at energies higher than the Mn d-orbitals. In Figure 3c, we show schematically that even if spin–orbit coupling would be considered, the Yb orbitals would probably lie above the conduction band, thus possibly preventing any energy transfer from the Mn d-orbitals, which we know absorb light from the PLE spectra of the doped systems. On the other hand, the $CsMnBr_3$ system presents a different electronic structure. The 1D connectivity among Mn and Yb octahedra moves the unoccupied f-orbital (spin-down) deep inside the band gap of the material, as shown in Figure 3e. The composition (in terms of atomic orbital contribution) of the unoccupied molecular orbitals (spin-down) localized on the $Yb^{3+}$ dopant(s) is provided in Tables S5–S7. Although the exact energetic position inside the gap is probably not well reproduced by DFT, we can safely assume that even after spin–orbit mixing, both $5f_{5/2}$ and $5f_{7/2}$ orbitals would still lie in the band gap, allowing emission from the dopant (Figure 3f). Additionally, we can also observe that the f-orbital is mixed with the 4p orbitals of Br, which are directly connected to the nearby Mn ions. This means that the conversion efficiency from Mn to Yb could be facilitated by electron–phonon coupling. A similar mechanism can be expected also from the other dopants.

In summary, we have introduced an optimized synthesis of $CsMnBr_3$ and $Cs_3MnBr_5$ NCs. Importantly, only $CsMnBr_3$ NCs could host different types of lanthanide ions and sensitize them via visible excitation, which was shown in our DFT calculations as well. As a result, sharp emissions at 890 and 1075 nm from $Nd^{3+}$, 1005 nm from $Yb^{3+}$, 1226 and 1489 nm from $Tm^{3+}$, and 1544 nm from $Er^{3+}$ were detected upon visible excitation of the $CsMnBr_3$ NCs matrix. This work provides a lead-free material as an efficient sensitizer, which can lead to development and design of visible-to-NIR downshifters.

## ■ EXPERIMENTAL METHODS

**Materials.** Cesium carbonate ($Cs_2(CO_3)$, 99%), manganese(II) acetate ($Mn(Ac)_2$, 98%), benzoyl bromide ($C_6H_5COBr$, 97%), oleic acid (OA, 90%), oleylamine (OAm, 98%), 1-octadecene (1-ODE, 90%), erbium(III) acetate hydrate ($Er(Ac)_3 \cdot H_2O$, 99.9%), ytterbium(III) acetate tetrahydrate ($Yb(Ac)_3 \cdot 4H_2O$, 99.9%), thulium(III) acetate hydrate ($Tm(Ac)_3 \cdot H_2O$, 99.9%), neodymium(III) acetate hydrate ($Nd(Ac)_3 \cdot H_2O$, 99.9%), ethyl acetate (99.9%), and toluene (99.7%) were purchased from Sigma-Aldrich and used without further purification.

**Synthesis of $CsMnBr_3$ NCs.** $Cs_2(CO_3)$ (65 mg), $Mn(Ac)_2$ (70 mg), OAm (1 mL), and OA (1 mL) were mixed in 1-ODE (2 mL). The solution was degassed at room temperature for 30 min and then filled with nitrogen. The solution was heated to 170 °C to form a clear mixture. Then, benzoyl bromide (450 $\mu$L in 0.5 mL toluene) was swiftly injected into the solution, and the reaction was quenched within 30 s using an ice–water bath. The crude solution was centrifuged at 4000 rpm for 5 min, and the precipitate was redispersed in toluene. The same washing procedure was repeated for three times.

**Synthesis of $Cs_3MnBr_5$ NCs.** $Cs_2(CO_3)$ (90 mg), $Mn(Ac)_2$ (70 mg), OAm (1 mL), and OA (1 mL) were mixed in 1-ODE (2 mL). The solution was degassed at room temperature for 30 min and then filled with nitrogen. The solution was heated to 210 °C to form a clear mixture. Then, benzoyl bromide (225 $\mu$L in 0.5 mL toluene) was swiftly injected into the solution, and the reaction was quenched within 30 s using an ice–water bath. The crude solution was centrifuged at 4000 rpm for 5 min, and the precipitate was redispersed in toluene. The same washing procedure was repeated three times.

**$Ln^{3+}$ Doping of $CsMnBr_3$ and $Cs_3MnBr_5$ NCs.** $Er(Ac)_3 \cdot H_2O$ (41 mg), $Yb(Ac)_3 \cdot 4H_2O$ (60 mg), $Tm(Ac)_3 \cdot H_2O$ (42 mg), and $Nd(Ac)_3 \cdot H_2O$ (40 mg) were introduced into the synthesis batch of $CsMnBr_3$ and $Cs_3MnBr_5$ NCs.

**X-ray Diffraction (XRD) Characterization.** XRD analysis was carried on a PANanalytical Empyrean X-ray diffractometer, equipped with a 1.8 kW Cu K$\alpha$ ceramic X-ray tube and a PIXcel3D 2×2 area detector, operating at 45 kV and 40 mA. A concentrated NC solution was drop-cast onto silicon zero-diffraction single-crystal substrate for the analysis, which was collected under ambient conditions using parallel beam geometry and symmetric reflection mode. The HighScore 4.1 software from PANalytical was used for data analysis.


https://doi.org/10.1021/acsenergylett.2c00311
ACS Energy Lett. 2022, 7, 1850–1858

**Transmission Electron Microscopy (TEM) Characterization.** TEM analysis was performed on a JEOL-1100 transmission electron microscope operating at an acceleration voltage of 100 kV. The dilute solutions of NCs were drop-cast onto carbon-coated copper grids. The TEM images were processed by the ImageJ software (https://imagej.nih.gov/ij/) for particle size determination. Scanning transmission electron microscopy (STEM) images were acquired on a ThermoFisher Spectra instrument operated at 300 kV using the high-angle annular dark field (HAADF) signal. EDS maps were acquired on a Dual-X setup with a total acquisition angle of 1.76 sr and processed with Velox.

**UV−Vis Absorption.** The UV−vis absorption spectra were recorded using a Varian Cary 300 UV−vis absorption spectrophotometer. Diluted NC solutions were dispersed in toluene in quartz cuvettes with a path length of 1 cm.

**Steady-State Optical Analyses.** The PLE, visible PL and NIR PL spectra were collected via an Edinburgh FLS900 fluorescence spectrometer equipped with a Xe lamp and a monochromator for steady-state PL excitation.

**Photoluminescence Quantum yield Measurements.** An Edinburgh FLS900 fluorescence spectrometer equipped with a Xe lamp, PMT-900 detector, PMT-1700 detector, and calibrated integrating sphere (N-M01) was used for PLQY measurement. Undoped samples were excited at 380 nm for the visible PLQY measurements, and doped samples were excited at 550 nm for the NIR PLQY measurements. The PLQY values were calculated by Flouracle software.

**Near-Infrared Photoluminescence Time Decay.** For transient PL measurements, the samples were excited using a Laser-export Co. Ltd., frequency-tripled, pulsed Nd:YAG laser at 355 nm (3.49 eV) with modulable repetition rate (from 1 kHz down to 150 Hz) and detected using a Oriel Instrument Cornerstone 1/4 m monochromator coupled with a Hamamatsu UV−vis photomultiplier and a Hamamatsu R5509 NIR photomultiplier tube cooled at liquid nitrogen temperature with a Products for Research, Inc. PC176TSCE005 cooling chamber.

**Density Functional Theory Calculations.** The band structure calculations of the undoped systems were performed using the VASP 5.4 package[81] at the DFT level using the PBE exchange−correlation functional[82] and without further inclusion of the spin−orbit coupling. We considered the tetragonal space group (SG) No. 140 for $Cs_3MnBr_5$ and the hexagonal SG No. 194 for $CsMnBr_3$ using, respectively, a 4×4×4 and a 6×6×6 k mesh grid for the Brillouin zone integration. All atomic positions and lattice parameters were relaxed until forces were <0.001 hartree/Å. We used a kinetic energy cutoff of 400 eV. To assess the impact of the magnetic behavior, we compared the stability of the pure ferromagnetic (five unpaired electrons on each Mn, spin-up) and pure antiferromagnetic (five unpaired electrons on each Mn, alternating spin-up and spin-down for adjacent Mn) configurations in both systems after structural relaxation. In order to investigate the effects of Yb-doping in both systems, we carried out atomistic simulations at the Γ point of the corresponding 2×2×2 supercells. In detail, we prepared a 2×2×2 $Cs_3MnBr_5$ supercell, replacing one $Mn^{2+}$ with one $Yb^{3+}$, and added a $Br^-$ ion to the corresponding tetrahedron in order to ensure the charge balance of our computational model (see Figure 3, upper right panel). Similarly, we built a 2×2×2 $CsMnBr_3$ supercell and replaced three neighboring (edge-connected) $Mn^{2+}$ respectively by an $Yb^{3+}$, a vacancy, and a $Yb^{3+}$ (see Figure 3, lower right panel). The structural relaxation and electronic structure calculation of such supercells were accomplished at the DFT/PBE level using a double-ζ basis set plus polarization functions on all atoms[83] as implemented in the CP2K 8.1 code.[84] Scalar relativistic effects have been incorporated as effective core potentials. Here, only the purely ferromagnetic (five unpaired electrons on each Mn, spin-up, and one unpaired electron on each Yb, spin-up) behavior was modeled.

## ■ ASSOCIATED CONTENT

### Supporting Information

The Supporting Information is available free of charge at https://pubs.acs.org/doi/10.1021/acsenergylett.2c00311.

EDS mapping data, UV−vis absorption and EDX spectra, PL decay lifetime values, and composition of the different orbitals of Yb-doped $CsMnBr_3$ and $Cs_3MnBr_5$ NCs, including Tables S1−S7 and Figures S1−S6 (PDF)

## ■ AUTHOR INFORMATION


### Corresponding Authors

**Liberato Manna** − *Department of Nanochemistry, Istituto Italiano di Tecnologia, 16163 Genova, Italy;* orcid.org/0000-0003-4386-7985; Email: liberato.manna@iit.it

**Francesco Di Stasio** − *Photonic Nanomaterials, Istituto Italiano di Tecnologia, 16163 Genova, Italy;* orcid.org/0000-0002-2079-3322; Email: francesco.distasio@iit.it

### Authors

**Houman Bahmani Jalali** − *Photonic Nanomaterials, Istituto Italiano di Tecnologia, 16163 Genova, Italy;* orcid.org/0000-0001-7212-9098

**Andrea Pianetti** − *Dipartimento di Scienza dei Materiali, Università degli Studi di Milano-Bicocca, 20125 Milano, Italy*

**Juliette Zito** − *Department of Nanochemistry, Istituto Italiano di Tecnologia, 16163 Genova, Italy; Dipartimento di Chimica e Chimica Industriale, Università degli Studi di Genova, 16146 Genova, Italy*

**Muhammad Imran** − *Department of Nanochemistry, Istituto Italiano di Tecnologia, 16163 Genova, Italy;* orcid.org/0000-0001-7091-6514

**Marta Campolucci** − *Dipartimento di Chimica e Chimica Industriale, Università degli Studi di Genova, 16146 Genova, Italy*

**Yurii P. Ivanov** − *Electron Spectroscopy and Nanoscopy, Istituto Italiano di Tecnologia, 16163 Genova, Italy*

**Federico Locardi** − *Dipartimento di Chimica e Chimica Industriale, Università degli Studi di Genova, 16146 Genova, Italy;* orcid.org/0000-0002-1794-8282

**Ivan Infante** − *Department of Nanochemistry, Istituto Italiano di Tecnologia, 16163 Genova, Italy;* orcid.org/0000-0003-3467-9376

**Giorgio Divitini** − *Electron Spectroscopy and Nanoscopy, Istituto Italiano di Tecnologia, 16163 Genova, Italy;* orcid.org/0000-0003-2775-610X

**Sergio Brovelli** − *Dipartimento di Scienza dei Materiali, Università degli Studi di Milano-Bicocca, 20125 Milano, Italy;* orcid.org/0000-0002-5993-855X

Complete contact information is available at: https://pubs.acs.org/10.1021/acsenergylett.2c00311




https://doi.org/10.1021/acsenergylett.2c00311
ACS Energy Lett. 2022, 7, 1850−1858

## Notes

The authors declare no competing financial interest.

## ACKNOWLEDGMENTS

We acknowledge support from the European Research Council project NANOLED (ERC-StG 851794) and the Ministry of University and Research (MIUR) through grant "Dipartimenti di Eccellenza—2017 Materials For Energy".

## REFERENCES

(1) Huang, X.; Han, S.; Huang, W.; Liu, X. Enhancing solar cell efficiency: the search for luminescent materials as spectral converters. *Chem. Soc. Rev.* **2013**, *42*, 173−201.

(2) Zhou, D.; Sun, R.; Xu, W.; Ding, N.; Li, D.; Chen, X.; Pan, G.; Bai, X.; Song, H. Impact of host composition, codoping, or tridoping on quantum-cutting emission of ytterbium in halide perovskite quantum dots and solar cell applications. *Nano Lett.* **2019**, *19*, 6904−6913.

(3) Zhou, D.; Liu, D.; Pan, G.; Chen, X.; Li, D.; Xu, W.; Bai, X.; Song, H. Cerium and ytterbium codoped halide perovskite quantum dots: a novel and efficient downconverter for improving the performance of silicon solar cells. *Adv. Mater.* **2017**, *29*, 1704149.

(4) Cai, T.; Wang, J.; Li, W.; Hills-Kimball, K.; Yang, H.; Nagaoka, Y.; Yuan, Y.; Zia, R.; Chen, O. $Mn^{2+}/Yb^{3+}$ codoped $CsPbCl_3$ Perovskite Nanocrystals with Triple-Wavelength Emission for Luminescent Solar Concentrators. *Adv. Sci.* **2020**, *7*, 2001317.

(5) Huang, H.; Li, R.; Jin, S.; Li, Z.; Huang, P.; Hong, J.; Du, S.; Zheng, W.; Chen, X.; Chen, D. Ytterbium-Doped $CsPbCl_3$ Quantum Cutters for Near-Infrared Light-Emitting Diodes. *ACS Appl. Mater. Interfaces* **2021**, *13*, 34561−34571.

(6) Zhong, Y.; Ma, Z.; Zhu, S.; Yue, J.; Zhang, M.; Antaris, A. L.; Yuan, J.; Cui, R.; Wan, H.; Zhou, Y.; et al. Boosting the down-shifting luminescence of rare-earth nanocrystals for biological imaging beyond 1500 nm. *Nat. Commun.* **2017**, *8*, 737.

(7) Zhang, H.; Fan, Y.; Pei, P.; Sun, C.; Lu, L.; Zhang, F. $Tm^{3+}$-Sensitized NIR-II Fluorescent Nanocrystals for *in vivo* Information Storage and Decoding. *Angew. Chem., Int. Ed.* **2019**, *58*, 10153−10157.

(8) Zhong, Y.; Ma, Z.; Wang, F.; Wang, X.; Yang, Y.; Liu, Y.; Zhao, X.; Li, J.; Du, H.; Zhang, M.; et al. *In vivo* molecular imaging for immunotherapy using ultra-bright near-infrared-IIb rare-earth nanoparticles. *Nat. Biotechnol.* **2019**, *37*, 1322−1331.

(9) Liu, L.; Wang, S.; Zhao, B.; Pei, P.; Fan, Y.; Li, X.; Zhang, F. $Er^{3+}$ Sensitized 1530 to 1180 nm Second Near-Infrared Window Upconversion Nanocrystals for *in vivo* Biosensing. *Angew. Chem.* **2018**, *130*, 7640−7644.

(10) Lei, X.; Li, R.; Tu, D.; Shang, X.; Liu, Y.; You, W.; Sun, C.; Zhang, F.; Chen, X. Intense near-infrared-II luminescence from $NaCeF_4$: Er/Yb nanoprobes for *in vitro* bioassay and *in vivo* bioimaging. *Chem. Sci.* **2018**, *9*, 4682−4688.

(11) Zhang, H.; Chen, Z.-H.; Liu, X.; Zhang, F. A mini-review on recent progress of new sensitizers for luminescence of lanthanide doped nanomaterials. *Nano Res.* **2020**, *13*, 1795−1809.

(12) Fan, Y.; Wang, P.; Lu, Y.; Wang, R.; Zhou, L.; Zheng, X.; Li, X.; Piper, J. A.; Zhang, F. Lifetime-engineered NIR-II nanoparticles unlock multiplexed *in vivo* imaging. *Nat. Nanotechnol.* **2018**, *13*, 941−946.

(13) Lu, Y.; Zhao, J.; Zhang, R.; Liu, Y.; Liu, D.; Goldys, E. M.; Yang, X.; Xi, P.; Sunna, A.; Lu, J.; et al. Tunable lifetime multiplexing using luminescent nanocrystals. *Nat. Photonics* **2014**, *8*, 32−36.

(14) Gu, Y.; Guo, Z.; Yuan, W.; Kong, M.; Liu, Y.; Liu, Y.; Gao, Y.; Feng, W.; Wang, F.; Zhou, J.; et al. High-sensitivity imaging of time-domain near-infrared light transducer. *Nat. Photonics* **2019**, *13*, 525−531.

(15) Hu, J.-Y.; Ning, Y.; Meng, Y.-S.; Zhang, J.; Wu, Z.-Y.; Gao, S.; Zhang, J.-L. Highly near-IR emissive ytterbium (III) complexes with unprecedented quantum yields. *Chem. Sci.* **2017**, *8*, 2702−2709.

(16) Moore, E. G.; Samuel, A. P.; Raymond, K. N. From antenna to assay: lessons learned in lanthanide luminescence. *Acc. Chem. Res.* **2009**, *42*, 542−552.

(17) Chengelis, D. A.; Yingling, A. M.; Badger, P. D.; Shade, C. M.; Petoud, S. Incorporating lanthanide cations with cadmium selenide nanocrystals: a strategy to sensitize and protect Tb (III). *J. Am. Chem. Soc.* **2005**, *127*, 16752−16753.

(18) Martín-Rodríguez, R.; Geitenbeek, R.; Meijerink, A. Incorporation and luminescence of $Yb^{3+}$ in CdSe nanocrystals. *J. Am. Chem. Soc.* **2013**, *135*, 13668−13671.

(19) Swabeck, J. K.; Fischer, S.; Bronstein, N. D.; Alivisatos, A. P. Broadband sensitization of lanthanide emission with indium phosphide quantum dots for visible to near-infrared downshifting. *J. Am. Chem. Soc.* **2018**, *140*, 9120−9126.

(20) Sadeghi, S.; Jalali, H. B.; Srivastava, S. B.; Melikov, R.; Baylam, I.; Sennaroglu, A.; Nizamoglu, S. High-performance, large-area, and ecofriendly luminescent solar concentrators using copper-doped InP quantum dots. *iScience* **2020**, *23*, 101272.

(21) Bahmani Jalali, H.; Sadeghi, S.; Baylam, I.; Han, M.; Ow-Yang, C. W.; Sennaroglu, A.; Nizamoglu, S. Exciton recycling via InP quantum dot funnels for luminescent solar concentrators. *Nano Res.* **2021**, *14*, 1488−1494.

(22) Bahmani Jalali, H.; Sadeghi, S.; Dogru Yuksel, I. B.; Onal, A.; Nizamoglu, S. Past, present and future of indium phosphide quantum dots. *Nano Res.* **2022**, DOI: 10.1007/s12274-021-4038-z.

(23) Song, D.; Chi, S.; Li, X.; Wang, C.; Li, Z.; Liu, Z. Upconversion system with quantum dots as sensitizer: improved photoluminescence and PDT efficiency. *ACS Appl. Mater. Interfaces* **2019**, *11*, 41100−41108.

(24) Jain, A.; Ong, S. P.; Hautier, G.; Chen, W.; Richards, W. D.; Dacek, S.; Cholia, S.; Gunter, D.; Skinner, D.; Ceder, G.; Persson, K. A. Commentary: The Materials Project: A materials genome approach to accelerating materials innovation. *APL Mater.* **2013**, *1*, 011002.

(25) Hu, Q.; Li, Z.; Tan, Z.; Song, H.; Ge, C.; Niu, G.; Han, J.; Tang, J. Rare Earth Ion-Doped $CsPbBr_3$ Nanocrystals. *Adv. Opt. Mater.* **2018**, *6*, 1700864.

(26) Milstein, T. J.; Kroupa, D. M.; Gamelin, D. R. Picosecond quantum cutting generates photoluminescence quantum yields over 100% in ytterbium-doped $CsPbCl_3$ nanocrystals. *Nano Lett.* **2018**, *18*, 3792−3799.

(27) Zeng, M.; Artizzu, F.; Liu, J.; Singh, S.; Locardi, F.; Mara, D.; Hens, Z.; Van Deun, R. Boosting the $Er^{3+}$ 1.5 $\mu$m luminescence in $CsPbCl_3$ perovskite nanocrystals for photonic devices operating at telecommunication wavelengths. *ACS Appl. Nano Mater.* **2020**, *3*, 4699−4707.

(28) Zeng, M.; Locardi, F.; Mara, D.; Hens, Z.; Van Deun, R.; Artizzu, F. Switching on near-infrared light in lanthanide-doped $CsPbCl_3$ perovskite nanocrystals. *Nanoscale* **2021**, *13*, 8118−8125.

(29) Mir, W. J.; Jagadeeswararao, M.; Das, S.; Nag, A. Colloidal Mn-doped cesium lead halide perovskite nanoplatelets. *ACS Energy Lett.* **2017**, *2*, 537−543.

(30) Pinchetti, V.; Anand, A.; Akkerman, Q. A.; Sciacca, D.; Lorenzon, M.; Meinardi, F.; Fanciulli, M.; Manna, L.; Brovelli, S. Trap-mediated two-step sensitization of manganese dopants in perovskite nanocrystals. *ACS Energy Lett.* **2019**, *4*, 85−93.

(31) Imran, M.; Ramade, J.; Di Stasio, F.; De Franco, M.; Buha, J.; Van Aert, S.; Goldoni, L.; Lauciello, S.; Prato, M.; Infante, I.; et al. Alloy $CsCd_xPb_{1-x}Br_3$ Perovskite Nanocrystals: The Role of Surface Passivation in Preserving Composition and Blue Emission. *Chem. Mater.* **2020**, *32*, 10641−10652.

(32) Lee, H.; Park, J.; Kim, S.; Lee, S.-C.; Kim, Y.-H.; Lee, T.-W. Perovskite Emitters as a Platform Material for Down-Conversion Applications. *Adv. Mater. Technol.* **2020**, *5*, 2000091.

(33) Abdelbar, M. F.; El-Kemary, M.; Fukata, N. Downshifting of highly energetic photons and energy transfer by Mn-doped perovskite $CsPbCl_3$ nanocrystals in hybrid organic/silicon nanostructured solar cells. *Nano Energy* **2020**, *77*, 105163.

(34) Fu, Z.; Xi, S. The effects of heavy metals on human metabolism. *Toxicol. Mech. Methods* **2020**, *30*, 167−176.

(35) Sobhanan, J.; Jones, P.; Kohara, R.; Sugino, S.; Vacha, M.; Subrahmanyam, C.; Takano, Y.; Lacy, F.; Biju, V. Toxicity of nanomaterials due to photochemical degradation and the release of heavy metal ions. *Nanoscale* **2020**, *12*, 22049−22058.

(36) Dey, A.; Ye, J.; De, A.; Debroye, E.; Ha, S. K.; Bladt, E.; Kshirsagar, A. S.; Wang, Z.; Yin, J.; Wang, Y. State of the Art and Prospects for Halide Perovskite Nanocrystals. *ACS Nano* **2021**, *15*, 10775−10981.

(37) Shamsi, J.; Urban, A. S.; Imran, M.; De Trizio, L.; Manna, L. Metal Halide Perovskite Nanocrystals: Synthesis, Post-Synthesis Modifications, and Their Optical Properties. *Chem. Rev.* **2019**, *119*, 3296−3348.

(38) Lee, W.; Hong, S.; Kim, S. Colloidal synthesis of lead-free silver−indium double-perovskite $Cs_2AgInCl_6$ nanocrystals and their doping with lanthanide ions. *J. Phys. Chem. C* **2019**, *123*, 2665−2672.

(39) Ding, N.; Zhou, D.; Pan, G.; Xu, W.; Chen, X.; Li, D.; Zhang, X.; Zhu, J.; Ji, Y.; Song, H. Europium-doped lead-free $Cs_3Bi_2Br_9$ perovskite quantum dots and ultrasensitive $Cu^{2+}$ detection. *ACS Sustainable Chem. Eng.* **2019**, *7*, 8397−8404.

(40) Mahor, Y.; Mir, W. J.; Nag, A. Synthesis and near-infrared emission of Yb-doped $Cs_2AgInCl_6$ double perovskite microcrystals and nanocrystals. *J. Phys. Chem. C* **2019**, *123*, 15787−15793.

(41) Chen, N.; Cai, T.; Li, W.; Hills-Kimball, K.; Yang, H.; Que, M.; Nagaoka, Y.; Liu, Z.; Yang, D.; Dong, A.; et al. Yb-and Mn-doped lead-free double perovskite $Cs_2AgBiX_6$ (X= $Cl^-$, $Br^-$) nanocrystals. *ACS Appl. Mater. Interfaces* **2019**, *11*, 16855−16863.

(42) Almutlaq, J.; Mir, W. J.; Gutiérrez-Arzaluz, L.; Yin, J.; Vasylevskyi, S.; Maity, P.; Liu, J.; Naphade, R.; Mohammed, O. F.; Bakr, O. M. $CsMnBr_3$: Lead-Free Nanocrystals with High Photoluminescence Quantum Yield and Picosecond Radiative Lifetime. *ACS Mater. Lett.* **2021**, *3*, 290−297.

(43) Shao, L.; Zhou, D.; Ding, N.; Sun, R.; Xu, W.; Wang, N.; Xu, S.; Liu, D.; Song, H. Broadband Ultraviolet Photodetectors Based on Cerium Doped Lead-Free $Cs_3MnBr_5$ Metal Halide Nanocrystals. *ACS Sustainable Chem. Eng.* **2021**, *9*, 4980−4987.

(44) Kong, Q.; Yang, B.; Chen, J.; Zhang, R.; Liu, S.; Zheng, D.; Zhang, H.; Liu, Q.; Wang, Y.; Han, K. Phase Engineering of Cesium Manganese Bromides Nanocrystals with Color-Tunable Emission. *Angew. Chem., Int. Ed.* **2021**, *133*, 19805−19811.

(45) Zhang, M.; Yue, J.; Cui, R.; Ma, Z.; Wan, H.; Wang, F.; Zhu, S.; Zhou, Y.; Kuang, Y.; Zhong, Y.; Pang, D.-W.; Dai, H. Bright quantum dots emitting at ∼ 1,600 nm in the NIR-IIb window for deep tissue fluorescence imaging. *Proc. Natl. Acad. Sci. U. S. A.* **2018**, *115*, 6590−6595.

(46) Seifert, H.; Kischka, K. Investigations on systems $AX/MnX_2$ (A= Li-Cs. TI: X= C1, Br, I) by DTA and X-ray analysis. *Thermochim. Acta* **1978**, *27*, 85−93.

(47) Imran, M.; Caligiuri, V.; Wang, M.; Goldoni, L.; Prato, M.; Krahne, R.; De Trizio, L.; Manna, L. Benzoyl halides as alternative precursors for the colloidal synthesis of lead-based halide perovskite nanocrystals. *J. Am. Chem. Soc.* **2018**, *140*, 2656−2664.

(48) Imran, M.; Mai, B. T.; Goldoni, L.; Cirignano, M.; Jalali, H. B.; Di Stasio, F.; Pellegrino, T.; Manna, L. Switchable Anion Exchange in Polymer-Encapsulated $APbX_3$ Nanocrystals Delivers Stable All-Perovskite White Emitters. *ACS Energy Lett.* **2021**, *6*, 2844−2853.

(49) De Franco, M.; Cirignano, M.; Cavattoni, T.; Jalali, H. B.; Prato, M.; Di Stasio, F. Facile purification protocol of $CsPbBr_3$ nanocrystals for light-emitting diodes with improved performance. *Opt. Mater.: X* **2022**, *13*, 100124.

(50) Goodyear, J.; Kennedy, D. The crystal structure of $CsMnBr_3$. *Acta Crystallogr., Sect. B: Struct. Crystallogr. Cryst. Chem.* **1972**, *28*, 1640−1641.

(51) Cox, D.; Merkert, F. The preparation, crystal growth and perfection of double halides of $CsNiCl_3$ type. *J. Cryst. Growth* **1972**, *13*, 282−284.

(52) Amit, M.; Horowitz, A.; Ron, E.; Makovsky, J. Preparation and Crystal Structures of Some Compounds of the $A_3$ $BX_5$ Type (A= Cs, Tl, $NH_4$, B= Mn, Fe, Co, X= Cl, Br). *Isr. J. Chem.* **1973**, *11*, 749−764.

(53) Linwood, S.; Weyl, W. The fluorescence of manganese in glasses and crystals. *J. Opt. Soc. Am.* **1942**, *32*, 443−453.

(54) Cotton, F. A.; Goodgame, D. M.; Goodgame, M. Absorption spectra and electronic structures of some tetrahedral manganese (II) complexes. *J. Am. Chem. Soc.* **1962**, *84*, 167−172.

(55) Morad, V.; Cherniukh, I.; Pöttschacher, L.; Shynkarenko, Y.; Yakunin, S.; Kovalenko, M. V. Manganese (II) in tetrahedral halide environment: factors governing bright green luminescence. *Chem. Mater.* **2019**, *31*, 10161−10169.

(56) Kambli, U.; Guedel, H. U. Transfer of electronic excitation energy in the antiferromagnets rubidium trichloromanganate (II), cesium trichloromanganate (II), cesium tribromomanganate (II), and rubidium tetrachloromanganate (II). *Inorg. Chem.* **1984**, *23*, 3479−3486.

(57) Rodríguez-Lazcano, Y.; Nataf, L.; Rodríguez, F. Electronic structure and luminescence of $[(CH_3)_4N]_2MnX_4$(X = Cl, Br) crystals at high pressures by time-resolved spectroscopy: Pressure effects on the Mn-Mn exchange coupling. *Phys. Rev. B* **2009**, *80*, 085115.

(58) Bai, X.; Zhong, H.; Chen, B.; Chen, C.; Han, J.; Zeng, R.; Zou, B. Pyridine-modulated Mn ion emission properties of $C_{10}H_{12}N_2MnBr_4$ and $C_5H_6NMnBr_3$ single crystals. *J. Phys. Chem. C* **2018**, *122*, 3130−3137.

(59) Lin, J.; Zhang, Q.; Wang, L.; Liu, X.; Yan, W.; Wu, T.; Bu, X.; Feng, P. Atomically precise doping of monomanganese ion into coreless supertetrahedral chalcogenide nanocluster inducing unusual red shift in $Mn^{2+}$ emission. *J. Am. Chem. Soc.* **2014**, *136*, 4769−4779.

(60) Orive, J.; Mesa, J. L.; Balda, R.; Fernández, J. n.; Rodríguez Fernández, J. s.; Rojo, T.; Arriortua, M. a. I. Enhancement of the luminescent properties of a new red-emitting phosphor, $Mn_2(HPO_3)F_2$, by Zn substitution. *Inorg. Chem.* **2011**, *50*, 12463−12476.

(61) Lv, Y.; Jin, Y.; Sun, T.; Su, J.; Wang, C.; Ju, G.; Chen, L.; Hu, Y. Visible to NIR down-shifting and NIR to visible upconversion luminescence in $Ca_{14}Zn_6Ga_{10}O_{35}$: $Mn^{4+}$, $Ln^{3+}$ (Ln = Nd,Yb,Er). *Dyes Pigm* **2019**, *161*, 137−146.

(62) Cotton, S. A.; Harrowfield, J. M. *Lanthanides: Coordination Chemistry in Encyclopedia of Inorganic and Bioinorganic Chemistry*; Wiley: New York, 2011.

(63) Marin, R.; Jaque, D. Doping lanthanide ions in colloidal semiconductor nanocrystals for brighter photoluminescence. *Chem. Rev.* **2021**, *121*, 1425−1462.

(64) Creutz, S. E.; Fainblat, R.; Kim, Y.; De Siena, M. C.; Gamelin, D. R. A selective cation exchange strategy for the synthesis of colloidal $Yb^{3+}$-doped chalcogenide nanocrystals with strong broadband visible absorption and long-lived near-infrared emission. *J. Am. Chem. Soc.* **2017**, *139*, 11814−11824.

(65) Gerner, P.; Wenger, O. S.; Valiente, R.; Güdel, H. U. Green and red light emission by upconversion from the near-IR in $Yb^{3+}$ doped $CsMnBr_3$. *Inorg. Chem.* **2001**, *40*, 4534−4542.

(66) Valiente, R.; Wenger, O. S.; Güdel, H. U. Upconversion luminescence in $Yb^{3+}$ doped $CsMnCl_3$: Spectroscopy, dynamics, and mechanisms. *J. Chem. Phys.* **2002**, *116*, 5196−5204.

(67) Valiente, R.; Wenger, O.; Güdel, H. U. New photon upconversion processes in $Yb^{3+}$ doped $CsMnCl_3$ and $RbMnCl_3$. *Chem. Phys. Lett.* **2000**, *320*, 639−644.

(68) Pan, G.; Bai, X.; Yang, D.; Chen, X.; Jing, P.; Qu, S.; Zhang, L.; Zhou, D.; Zhu, J.; Xu, W.; et al. Doping lanthanide into perovskite nanocrystals: highly improved and expanded optical properties. *Nano lett* **2017**, *17*, 8005−8011.

(69) Mir, W. J.; Sheikh, T.; Arfin, H.; Xia, Z.; Nag, A. Lanthanide doping in metal halide perovskite nanocrystals: spectral shifting, quantum cutting and optoelectronic applications. *NPG Asia Mater.* **2020**, *12*, 9.

(70) Mir, W. J.; Mahor, Y.; Lohar, A.; Jagadeeswararao, M.; Das, S.; Mahamuni, S.; Nag, A. Postsynthesis doping of Mn and Yb into $CsPbX_3$(X = Cl,Br, or I) perovskite nanocrystals for downconversion emission. *Chem. Mater.* **2018**, *30*, 8170−8178.

(71) Song, P.; Hase, S.; Zhao, S.; Xu, Z.; Iso, Y.; Isobe, T. Feasibility of Emission-Enhanced $CsPbCl_3$ Quantum Dots Co-Doped with $Mn^{2+}$


https://doi.org/10.1021/acsenergylett.2c00311
*ACS Energy Lett.* 2022, 7, 1850−1858

and $Er^{3+}$ as Luminescent Downshifting Layers in Crystalline Silicon Solar Modules. *ACS Appl. Nano Mater.* **2022**, *5*, 2522−2531.
(72) Ouyang, Y.; Jiang, X.; Jiang, F.; Li, L.; Zhao, H.; Zhang, C.; Zheng, M.; Zheng, W.; Jiang, Y.; Zhu, X.; et al. Light-Soaking Induced Optical Tuning in Rare Earth-Doped All-Inorganic Perovskite. *Adv. Funct. Mater.* **2022**, *32*, 2107086.
(73) Zhao, Y.; Xie, C.; Zhang, X.; Matras-Postolek, K.; Yang, P. Mn: $CsPbBr_3$ Nanoplatelets for Bright White-Emitting Displays. *ACS Appl. Nano Mater.* **2021**, *4*, 6223−6230.
(74) Shannon, R. Revised effective ionic radii and systematic studies of interatomic distances in halides and chalcogenides. *Acta Crystallogr.* **1976**, *32*, 751−767.
(75) Deng, D.; Xu, S.; Zhao, S.; Li, C.; Wang, H.; Ju, H. Enhancement of upconversion luminescence in $Tm^{3+}/Er^{3+}/Yb^{3+}$-codoped glass ceramic containing $LiYF_4$ nanocrystals. *J. Lumin.* **2009**, *129*, 1266−1270.
(76) Zhang, X.; Zhang, Y.; Zhang, X.; Yin, W.; Wang, Y.; Wang, H.; Lu, M.; Li, Z.; Gu, Z.; Yu, W. W. $Yb^{3+}$ and $Yb^{3+}/Er^{3+}$ doping for near-infrared emission and improved stability of $CsPbCl_3$ nanocrystals. *J. Mater. Chem. C* **2018**, *6*, 10101−10105.
(77) Talluto, K. F.; Trautmann, V. F.; McPherson, G. L. Energy transfer in linear chain manganese salts: Emission spectra of $CsMnBr_3$, $RbMnBr_3$ and $CsMnI_3$ crystals doped with $Er^{3+}$. *Chem. Phys.* **1984**, *88*, 299−307.
(78) McPherson, G. L.; Waguespack, Y. Y.; Vanoy, T. C.; Rodriguez, W. J. Exciton migration in a "pseudo"-one-dimensional crystal: Luminescence dynamics of doped $CsMnBr_3$. *J. Chem. Phys.* **1990**, *92*, 1768−1774.
(79) Eremenko, V.; Karachevtsev, V.; Shapiro, V.; Slavin, V. Low-temperature transport of magnetic excitons in the quasi-one-dimensional antiferromagnet $CsMnCl_3{\cdot}2H_2O$ doped with $Cu^{2+}$ ions. *Phys. Rev. B* **1996**, *54*, 447.
(80) McPherson, G. L.; Francis, A. Extensive Energy Transfer in a Nearly One-Dimensional Crystal: The Emisson Spectrum of $CsMnBr_3$ Doped with $Nd^{3+}$. *Phys. Rev. Lett.* **1978**, *41*, 1681.
(81) Kresse, G.; Furthmüller, J. Efficient iterative schemes for ab initio total-energy calculations using a plane-wave basis set. *Phys. Rev. B* **1996**, *54*, 11169.
(82) Perdew, J. P.; Burke, K.; Ernzerhof, M. Generalized gradient approximation made simple. *Phys. Rev. Lett.* **1996**, *77*, 3865.
(83) VandeVondele, J.; Hutter, J. Gaussian basis sets for accurate calculations on molecular systems in gas and condensed phases. *J. Chem. Phys.* **2007**, *127*, 114105.
(84) Hutter, J.; Iannuzzi, M.; Schiffmann, F.; VandeVondele, J. cp2k: atomistic simulations of condensed matter systems. *Wiley Interdiscip. Rev.: Comput. Mol. Sci.* **2014**, *4*, 15−25.


https://doi.org/10.1021/acsenergylett.2c00311
*ACS Energy Lett.* 2022, 7, 1850−1858

SUPPORTING INFORMATION

# Cesium Manganese Bromide Nanocrystal Sensitizers for Broadband Vis-to-NIR Downshifting

*Houman Bahmani Jalali[a], Andrea Pianetti[b], Juliette Zito[c,d], Muhammad Imran[c], Marta Campolucci[d], Yurii P. Ivanov[e], Federico Locardi[d], Ivan Infante[c], Giorgio Divitini[e], Sergio Brovelli[b], Liberato Manna[c]*, and Francesco Di Stasio [a]**

[a] Photonic Nanomaterials group, Istituto Italiano di Tecnologia, Via Morego 30, 16163 Genova, Italy

[b] Dipartimento di Scienza dei Materiali, Università degli Studi di Milano-Bicocca, Via R. Cozzi 55, 20125 Milano, Italy

[c] Department of Nanochemistry, Istituto Italiano di Tecnologia, Via Morego 30, 16163 Genova, Italy

[d] Dipartimento di Chimica e Chimica Industriale, Università degli Studi di Genova, 16146 Genova, Italy

[e] Electron Spectroscopy and Nanoscopy, Istituto Italiano di Tecnologia, Via Morego 30, 16163 Genova, Italy

**Table S1.** HAADF STEM EDS mapping data of the $CsMnBr_3$ and $Cs_3MnBr_5$ NCs.

| **Element** | **$Cs_3MnBr_5$** | **$CsMnBr_3$** |
|---|---|---|
| **Cs (at. %)** | 31 ± 3 | 18 ± 2 |
| **Mn (at. %)** | 13 ± 1 | 19 ± 2 |
| **Br (at. %)** | 57 ± 4 | 63 ± 3 |

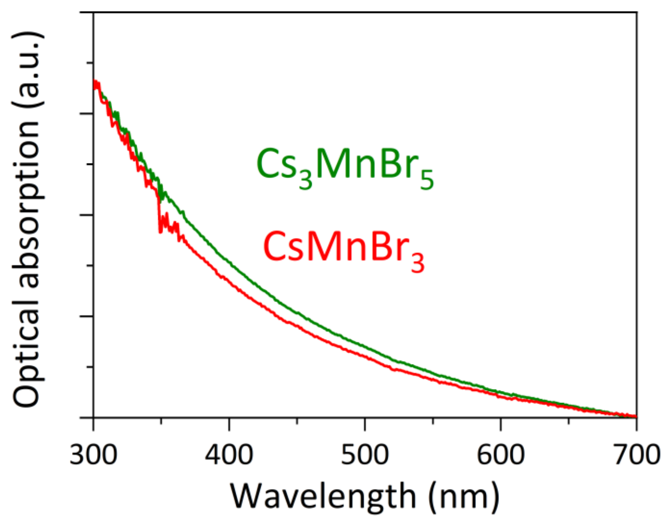


**Figure S1.** UV/Visible absorption of the $Cs_3MnBr_5$ (green) and $CsMnBr_3$ (red) NCs dispersed in toluene.

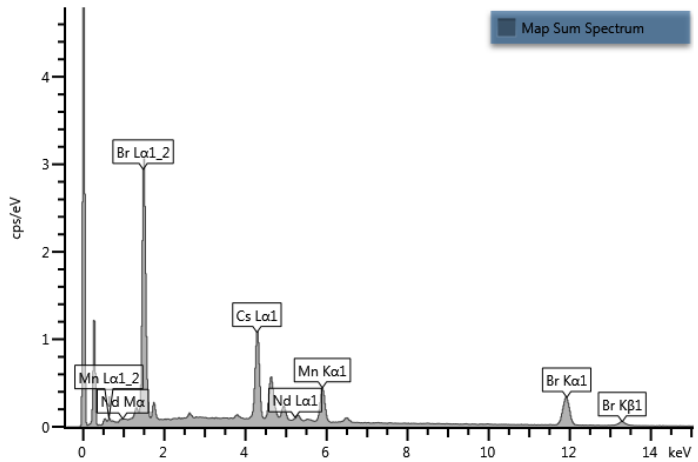


**Figure S2.** EDX spectrum recording from Nd doped $Cs_3MnBr_5$ NCs, showing the existence of Cs, Mn and Br elemental signals

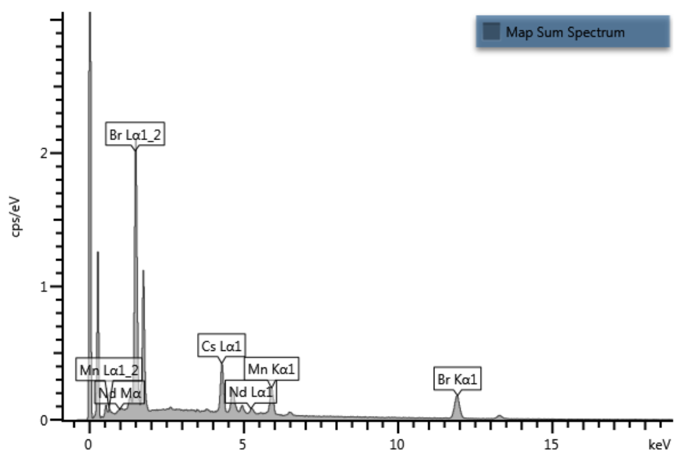


**Figure S3.** EDX spectrum recording from Nd doped $CsMnBr_3$ NCs, showing the existence of Cs, Mn, Br and Nd elemental signals

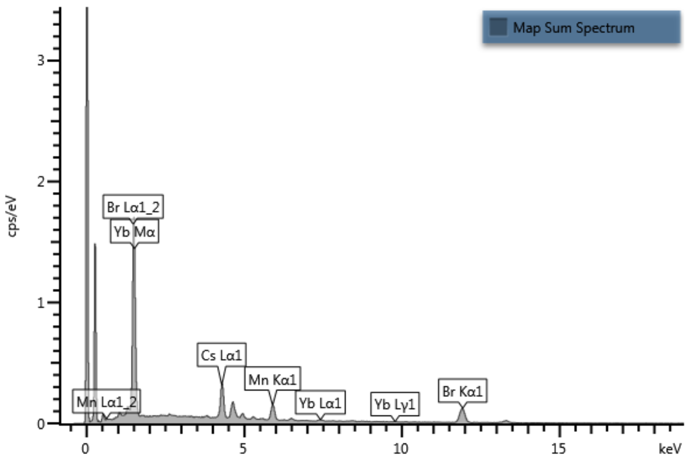


**Figure S4.** EDX spectrum recording from Yb doped $CsMnBr_3$ NCs, showing the existence of Cs, Mn, Br and Yb elemental signals

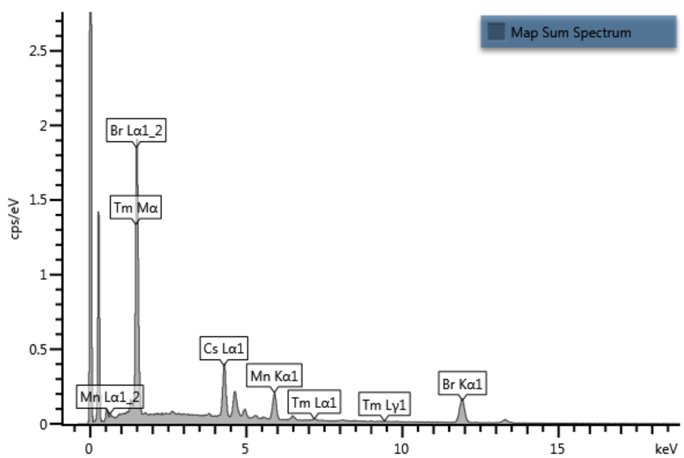


**Figure S5.** EDX spectrum recording from Tm doped $CsMnBr_3$ NCs, showing the existence of Cs, Mn, Br and Tm elemental signals

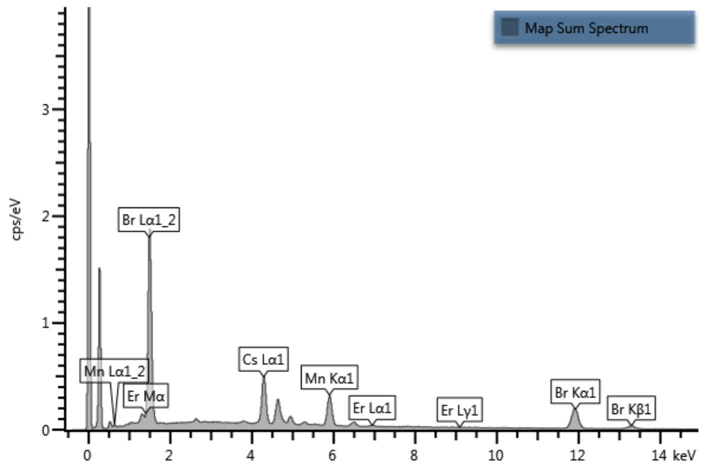


**Figure S6.** EDX spectrum recording from Er doped $CsMnBr_3$ NCs, showing the existence of Cs, Mn, Br and Er elemental signals

**Table S2.** Visible PL decay lifetimes of the $CsMnBr_3$ and $Cs_3MnBr_5$ NCs.

| Sample | Emission wavelength (nm) | Lifetime (τ) |
|---|---|---|
| $CsMnBr_3$ NCs | 661 | 235 µs |
| $Cs_3MnBr_5$ NCs | 522 | 170 µs |

**Table S3.** NIR PL decay lifetimes of the $Ln^{3+}$ doped $CsMnBr_3$ NCs.

| Dopant | Emission wavelength (nm) | Lifetime (τ) |
|---|---|---|
| $Nd^{3+}$ doped $CsMnBr_3$ NCs | 895 | 810 µs |
| $Tm^{3+}$ doped $CsMnBr_3$ NCs | 1230 | 1.4 ms |
| $Yb^{3+}$ doped $CsMnBr_3$ NCs | 990 | 730 µs |

**Table S4.** NIR PLQY of the $Ln^{3+}$ doped $CsMnBr_3$ NCs.

| Dopant | NIR PLQY (%) |
|---|---|
| $Nd^{3+}$ doped $CsMnBr_3$ NCs | 0.41 |
| $Tm^{3+}$ doped $CsMnBr_3$ NCs | 0.63 |
| $Yb^{3+}$ doped $CsMnBr_3$ NCs | 1.1 |
| $Er^{3+}$ doped $CsMnBr_3$ NCs | 0.24 |

**Table S5.** Atomic composition projected on each atomic orbital type for the MO in Yb doped $CsMnBr_3$ NCs localized on the the Yb ion.

| atomic kind | s | p | d | f | g |
|---|---|---|---|---|---|
| Cs | 0.021328 | 0.005641 | 0.005500 | - | - |
| Mn | 0.002126 | 0.000292 | 0.003116 | 0.000582 | - |
| Br | 0.014030 | 0.010663 | 0.005542 | - | - |
| Yb | 0.003467 | 0.001281 | 0.010993 | 0.914558 | 0.000883 |

**Table S6.** Atomic composition projected on each atomic orbital type for the LUMO (spin-down) in Yb doped $Cs_3MnBr_5$ NCs. The MO is localized on the second Yb ion.

| atomic kind | s | p | d | f | g |
|---|---|---|---|---|---|
| Cs | 0.001342 | 0.002716 | 0.001417 | - | - |
| Mn | 0.000073 | 0.000324 | 0.001326 | 0.000885 | - |
| Br | 0.001135 | 0.170221 | 0.002162 | - | - |
| Yb | 0.000050 | 0.004023 | 0.001001 | 0.809748 | 0.003579 |

**Table S7.** Atomic composition projected on each atomic orbital type for the LUMO+1 (spin-down) in Yb doped $Cs_3MnBr_5$ NCs. The MO is localized on the second Yb ion.

| atomic kind | s | p | d | f | g |
|---|---|---|---|---|---|
| Cs | 0.001008 | 0.001856 | 0.001148 | - | - |
| Mn | 0.000150 | 0.000218 | 0.002205 | 0.000948 | - |
| Br | 0.000982 | 0.122471 | 0.002427 | - | - |
| Yb | 0.000392 | 0.003297 | 0.001284 | 0.859343 | 0.002271 |